Chapter 3
Model Calculation

3.1 Introduction

As shown in Chaps. 4–8, the disk and envelope components associated to the protostar and the bipolar outflow launched from the vicinity of the protostar are detected. These components are heavily contaminated with one another, and thus their disentanglement is essential to investigate the geometrical and kinematic structure around the protostar. For this purpose, models of an envelope, a disk, and an outflow are employed to calculate their kinematic structure to disentangle the contaminated components obtained in the observations. Moreover, the models are useful to evaluate physical parameters, such as the protostellar mass, the specific angular momentum of the gas, and the inclination angle.

It is generally thought that the mid-plane of the disk/envelope system and the outflow axis are almost perpendicular to each other. Their configuration thus can be constrained if one of them is characterized. In Chaps. 4–8, the characterization is started with the component detected more clearly in each source. For instance, the disk/envelope system is more clearly delineated than the outflow component in L1527 (Chap. 4), while the outflow is more clearly delineated in IRAS 15398−3359 (Chap. 5).

3.2 Infalling-Rotating Envelope Model

3.2.1 Configuration of the Infalling-Rotating Envelope Model

A ballistic model is constructed to investigate infalling-rotating envelopes [7]. The basic concept of this model is introduced to explain the kinematic structure of the infalling-rotating envelope of L1527 [11]. Here, it is improved to consider the velocity

Y. Oya, *A Few Tens au Scale Physical and Chemical Structures Around Young Low-Mass Protostars*, Springer Theses, https://doi.org/10.1007/978-981-19-1708-0_3

field in the three dimensional space with the convolution by the beam size and the velocity resolution.

Figure 3.1 shows the schematic illustration of the 'infalling-rotating envelope' model. In this model, the gas is simply assumed to be falling and rotating under the gravity of the central protostar. The motion of the gas is approximated by the particle motion, ignoring effects of gas pressure, magnetic field, self gravity, and so on. Because of the energy and angular momentum conservation, the gas cannot fall inward of a certain radius, or the 'perihelion'. This position is called as 'centrifugal barrier'. The radius of the centrifugal barrier ($r_{\rm CB}$) is represented as:

$$r_{\rm CB} = \frac{j^2}{2GM}, \tag{3.1}$$

where G is the gravitational constant, M is the protostellar mass, and j is the specific angular momentum of the gas. It is the radius at which all the kinetic energy is converted to the rotational energy. It is a half of the centrifugal radius ($r_{\rm CR}$), where the gravitational force and the centrifugal force balance each other out:

$$\begin{aligned} r_{\rm CR} &= \frac{j^2}{GM} \\ &= 2r_{\rm CB}. \end{aligned} \tag{3.2}$$

The rotation and infall velocities ($v_{\rm rot}$ and $v_{\rm fall}$) of the gas at the distance of r to the protostar are represented as follows:

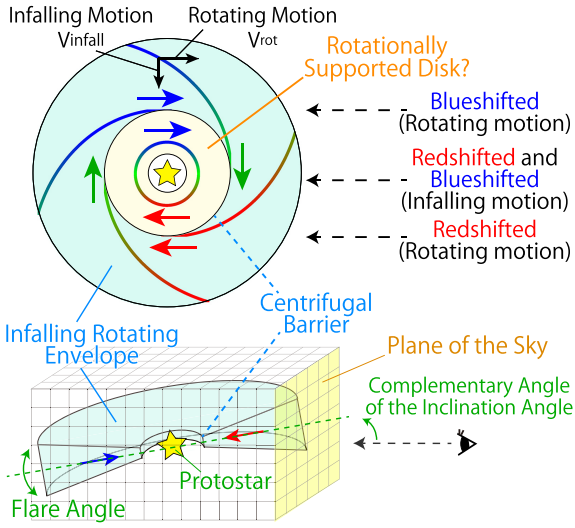

Fig. 3.1 Schematic illustration of the infalling-rotating envelope model. The space and the velocity field are sectioned into meshes

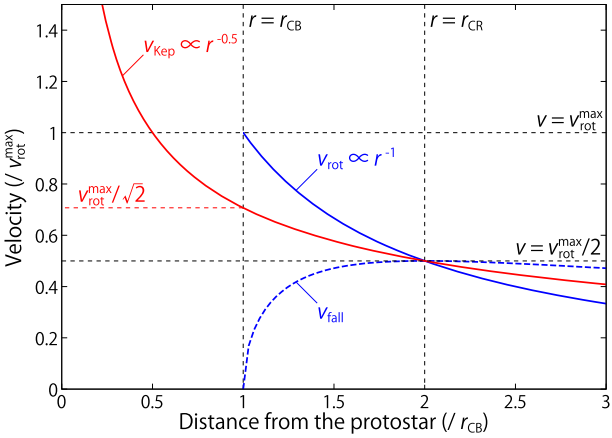

Fig. 3.2 The velocity of the gas in the infalling-rotating envelope and Keplerian disk model as a function of the distance from the protostar. The horizontal axis represents the distance from the protostar (r) normalized by the radius of the centrifugal barrier (r_{CB}), and the vertical axis represents the velocity (v) normalized by the rotation velocity of the infalling-rotating envelope model at the centrifugal barrier $\left(v_{rot}^{max}\right)$. The blue solid and dashed lines represent the rotation (v_{rot}) and infall (v_{fall}) velocities of the infalling-rotating envelope model. v_{fall} equals 0 at the centrifugal barrier ($r = r_{CB}$), and v_{rot} takes its maximum value there. On the other hand, v_{fall} takes the maximum value at the centrifugal radius ($r_{CR} = 2r_{CB}$). The red solid line represents the Keplerian velocity (v_{Kep}). All of v_{rot}, v_{fall}, and v_{Kep} take the same value $\left(v = v_{rot}^{max}/2\right)$ at the centrifugal radius (r_{CR})

$$
\begin{aligned}
v_{rot} &= \frac{j}{r} \\
&= \frac{1}{r}\sqrt{2GMr_{CB}}, \qquad (3.3) \\
v_{fall} &= \sqrt{\frac{2GM}{r} - v_{rot}^2} \\
&= \frac{1}{r}\sqrt{2GM\,(r - r_{CB})}. \qquad (3.4)
\end{aligned}
$$

Thus, the velocity field is determined by M and r_{CB}. The inclination angle (i) of the disk/envelope system also affects the apparent velocity along the line of sight. At the centrifugal barrier, v_{fall} equals to 0, and v_{rot} takes its maximum value. On the other hand, v_{fall} takes its maximum value at the centrifugal radius. The values of v_{rot} and v_{fall} as a function of the radius from the protostar are plotted in Fig. 3.2.

In this model, the distribution of the gas is assumed to have a power-law. The power-law of $r^{-1.5}$ corresponds to the density profile of an infalling cloud (e.g. [3, 6, 13]). An optically thin condition is also assumed, where the intensity of the line emission is proportional to the column density along the line of sight. Namely, excitation effects and radiative transfer effects are not considered. These assumptions are rather arbitrary in this study, because the main interest in the model analysis is on the velocity field of the gas around the protostar.

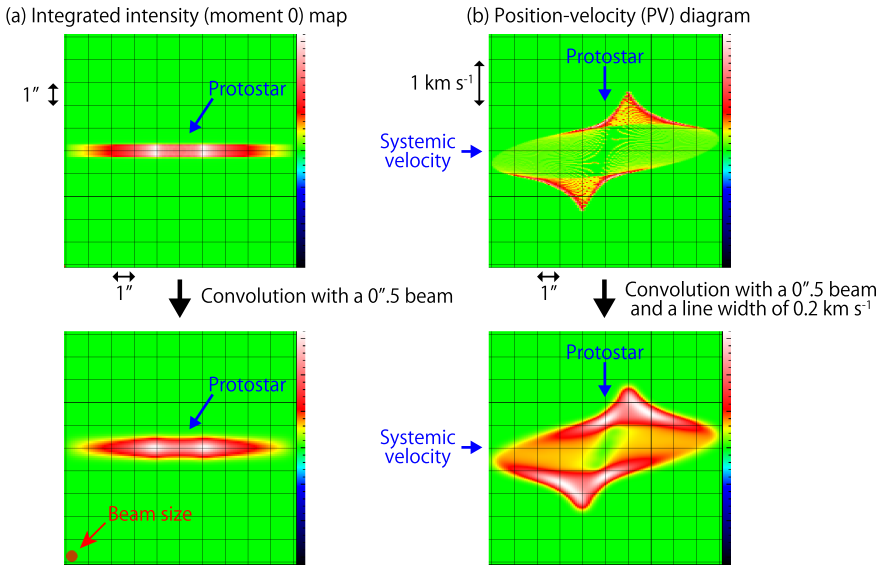

Fig. 3.3 Effects of the convolution of the line emission with an intrinsic Gaussian profile (FWHM = 0.2 km s^{-1}) and a Gaussian beam (0″.5 × 0″.5) in the infalling-rotating envelope model. The color scales represent the intensity of the line emission. Panels **a** and **b** show the integrated intensity map and the position velocity (PV) diagram along the disk/envelope system, respectively. In these models, the inclination angle (i) of 90° (an edge-on configuration) is employed for simplicity

The spectral line is assumed to have an intrinsic Gaussian profile with a certain line width, and the emission is convolved with a Gaussian beam with a certain full width at half maximum (FWHM) (Fig. 3.3). The intrinsic line width and the beam size are employed depending on each source. The mesh sizes are also appropriately chosen for each source.

Figure 3.4 shows an example of the results of the infalling-rotating envelope model. Its physical parameters are summarized in the caption. Figure 3.4a shows the integrated intensity map. The envelope is assumed to have an edge-on configuration extended along the east-west axis, where the left- and right-hand sides correspond to east and west, respectively. The integrated intensity relative to its peak value in the panel is shown in a color scale. The protostar with a mass (M) of 0.1 $M_\odot$ exists at the central position in Fig. 3.4a. The distance to the source from the Sun (d) is set to be 100 pc, where 1″ corresponds to 100 au. The envelope has an outer radius (R) of 500 au, outside which there is no molecule. The radius of the centrifugal barrier is 100 au, and the molecular density is zero inside the centrifugal barrier. The integrated intensity is the highest around the centrifugal barrier.

Figure 3.4b shows the position-velocity (PV) diagram along the blue arrow shown in Fig. 3.4a. The angular offset of 0″ corresponds to the protostellar position. The vertical axis represents the line-of-sight velocity of the molecules relative to the systemic velocity of the source. In Fig. 3.4b, a spin-up feature can be seen along the

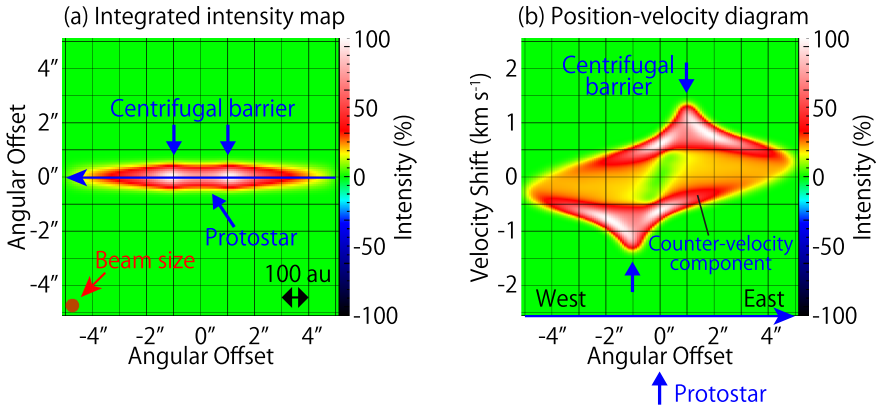

Fig. 3.4 The results of the infalling-rotating envelope model. Panels **a** and **b** show its integrated intensity map and position-velocity diagram, respectively. The position axis in panel (**b**) is taken along the blue horizontal arrow shown in panel (**a**), along which the mid-plane of the envelope is extended. The physical parameters of the model is as follows; the distance to the source from the Sun (d) of 100 pc, the protostellar mass (M) of 0.1 $M_\odot$, the radius of the centrifugal barrier ($r_{\rm CB}$) of 100 au, the inclination angle of the disk/envelope system (i) of 90° (0° for a face-on configuration), and the outer radius of the envelope (R) of 500 au. The scale height of the envelope is assumed to be 50 au independent of the radius. The mesh size for the calculation is 0.″08 (8 au), and 128 × 128 × 128 meshes are applied to cover the cubic space of 10.″24 × 10.″24 × 10.″24 (1024 × 1024 × 1024 au^3). The mesh size for the velocity axis is 0.02 km s^{-1}, and 256 meshes are applied to cover the velocity range from −2.56 km s^{-1} to 2.56 km s^{-1}. The intensity is convolved with the intrinsic line width of 0.2 km s^{-1} and the beam of 0.″5×0.″5

east-west axis; the rotation velocity of the molecules increases as approaching to the protostar till the centrifugal barrier. The velocity takes its maximum and minimum values around the centrifugal barrier, where the velocity is positive (red-shifted) and negative (blue-shifted) in the eastern and western sides of the protostar, respectively. Toward the protostellar position, only a velocity shift due to the infall motion can be seen. The infall motion can also be confirmed as the counter velocity component (Fig. 3.4b).

3.2.2 *Infalling-Rotating Envelope Model with Various Physical Parameters*

In this study, the physical parameters of low-mass protostellar sources are evaluated by comparing the observed kinematic structure of the gas and the infalling-rotating envelope model. For this purpose, it is demonstrated how sensitive to the physical parameters the model results are for some cases.

The infalling-rotating envelope model has three major physical parameters; M, $r_{\rm CB}$, and i. The apparent distribution of the line emission projected onto the plane of the sky is determined by $r_{\rm CB}$ and i. Figure 3.5 shows the integrated intensity

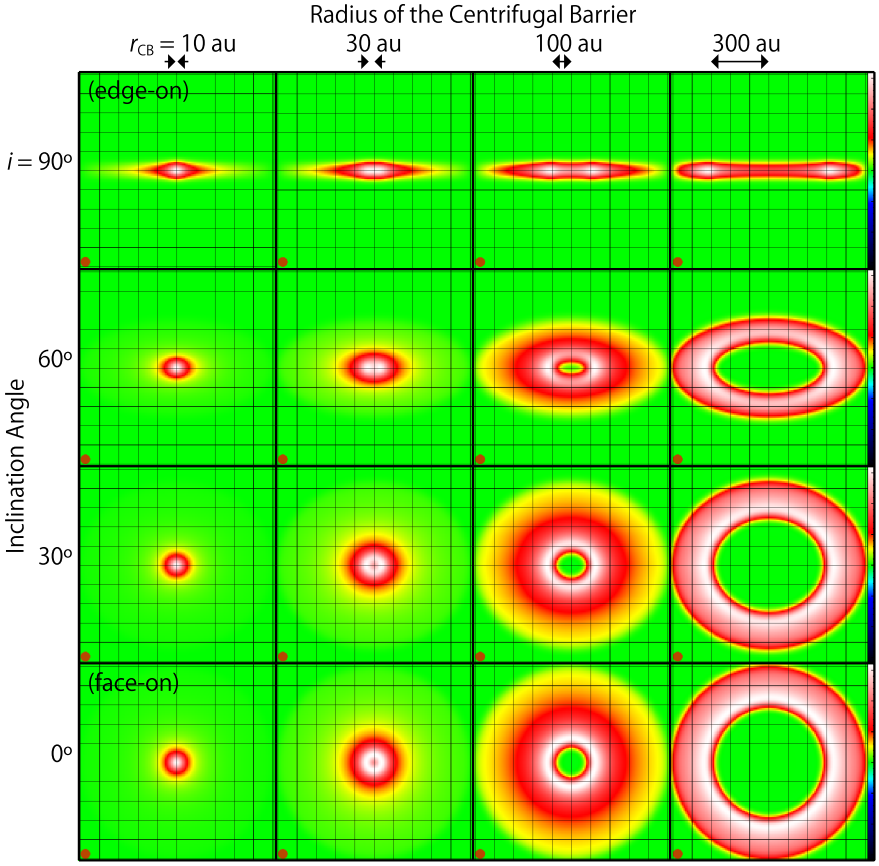

Fig. 3.5 Integrated intensity (moment 0) maps of the infalling-rotating envelope model with various sets of the radius of the centrifugal barrier (r_{CB}) and the inclination angle of the disk/envelope system (i). The other physical parameters for the models are set as follows; the distance from the Sun d = 100 pc, the protostellar mass $M = 0.1\ M_{\odot}$, and the outer radius of the envelope R = 500 au. The FWHM values of the intrinsic line width and the Gaussian beam are set to be 0.2 km s^{-1} and 0.″5, respectively. The uniform scale height of the envelope of 50 au is assumed. The mesh sizes are set to be 0.″08 and 0.01 km s^{-1}

maps for various sets of r_{CB} and i. Here, i of 0° and 90° corresponds to face-on and edge-on configurations, respectively. The FWHM value of the Gaussian beam (angular resolution) is 0.″5 (50 au). The other physical parameters are summarized in the caption of Fig. 3.5. With the edge-on configuration (i = 90°), the integrated intensity maps show a flattened feature. The maps with r_{CB} of 10 and 30 au show single-peaked distributions. Their centrifugal barriers seem to be almost unresolved with the beam of 0.″5. On the other hand, the maps with r_{CB} of 100 and 300 au show double-peaked distributions. The peak positions seem to correspond to the positions of their centrifugal barriers; namely, their centrifugal barriers are spatially resolved

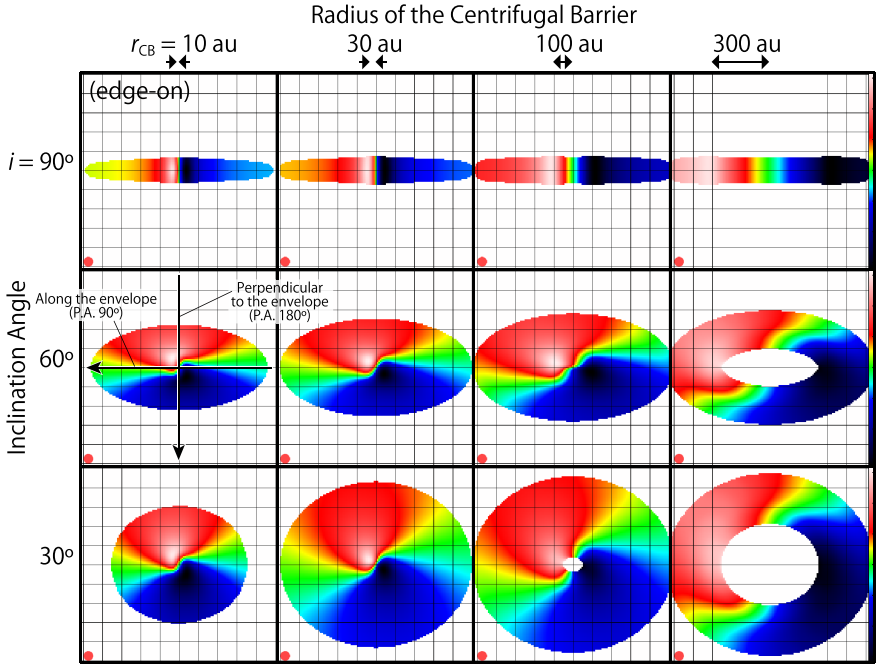

Fig. 3.6 Maps of the velocity field (moment 1 maps) of the infalling-rotating envelope model with various sets of r_{CB} and i. The other physical parameters are set to be as the same as those in Fig. 3.5. The color scale represents the averaged velocity-shift (Eq. 3.5). The color maps are shown only at the positions where the integrated intensity (Fig. 3.5) is larger than 1% of the peak integrated intensity. Thus, the data at the positions with a weaker integrated intensity than this criteria are shown in white. The black arrows in the panel with r_{CB} of 10 au and i of 60° represent the directions along which the PV diagrams in Figs. 3.7, 3.8 and 3.9 are prepared

with the beam. At i of 60° (nearly edge-on), the hole of the distribution is clearly seen in the panels for r_{CB} of 100 and 300 au. Although the model for r_{CB} of 30 au does not show a clear double-peaked distribution at i of 60°, it shows an intensity dip toward the protostar at i of 30° (nearly face-on). With the face-on configuration (i = 0°), the distributions show completely circular or ring-like structures. The intensities have their maximum value around the centrifugal barriers.

The velocity field of the gas is determined by M, r_{CB}, and i. The velocity along the line of sight (v_{shift}) in each mesh is calculated to compare with observations. Figure 3.6 shows the moment 1 maps with the various sets of r_{CB} and i. The FWHM value of the Gaussian beam is 0.″5 (50 au). The other physical parameters are summarized in its caption. The color map represents the average velocity shift weighted by the intensity ($\bar{v}$). It is calculated by using the following equation:

$$\bar{v} = \frac{\int vI(v)dv}{\int I(v)dv}, \tag{3.5}$$

where $I(v)$ denotes the intensity at the velocity v at the position. The denominator in the Eq. (3.5) corresponds to the integrated intensity at the position. Thus, the averaged velocity at a position having an infinitesimal integrated intensity has no sense. Hence, the data at the positions with integrated intensities smaller than the 1% relative to the peak integrated intensity are dropped in Fig. 3.6, and they are shown in white in the moment 1 maps. With the edge-on configuration ($i = 90°$), the averaged velocity in the eastern and western side of the protostar is red- and blue-shifted, respectively. These velocity shifts represent the rotation motion around the protostar. The maximum velocity shift is seen around the centrifugal barrier. The velocity does not show any gradient along the north-south axis.

On the other hand, velocity gradients along the north-south axis are seen in the panels for i of 30° and 60°. These velocity gradients are due to the infall motion. In these models, the southern side of the envelopes face to us, and thus the line emission is red-shifted in the northern side of the protostar, where the molecules are in front of the protostar. In these panels, the velocity fields show skewed features; the most blue- and red-shifted components are seen in the southwestern and northeastern sides of the protostar, respectively, where the projected velocity components of the rotation and infall motions have the same direction along the line of sight. With the face-on configuration ($i = 0°$), the velocity shift is completely symmetric to the mid-plane of the envelope, and thus the average velocity is zero everywhere. The value of $v_{\rm shift}$ is proportional to M as shown in the Eqs. (3.3) and (3.4). Thus, M does not affect the moment 1 map in appearance.

Figure 3.7 shows the position-velocity (PV) diagrams along the arrows shown in Fig. 3.6. The position axes are taken along the direction where the mid-plane of the envelopes are extended (Fig. 3.6). In Fig. 3.7, $r_{\rm CB}$ and i are varied to show how sensitive to these physical parameters the model results are. The FWHM value of the Gaussian beam is 0.″5 (50 au). The other physical parameters are summarized in the caption. With the edge-on configuration ($i = 90°$), the spin-up feature toward the centrifugal barrier is seen with all $r_{\rm CB}$. The maximum velocity-shift seen at the centrifugal barrier is larger for a smaller $r_{\rm CB}$. Although the centrifugal barriers are not spatially resolved in the integrated intensity maps for $r_{\rm CB}$ of 10 and 30 au (Fig. 3.5), a velocity gradient is visible between the positions of the centrifugal barriers in their PV diagrams. The infall motion can be confirmed as the counter velocity components. The velocity shifts toward the protostellar position also reflect the infall motion. With i of 30° and 60°, the counter velocity components are not seen for $r_{\rm CB}$ of 100 and 300 au, while they can be seen with $r_{\rm CB}$ of 10 and 30 au. The infall gas in the models with $r_{\rm CB}$ of 100 and 300 au are distant from the protostellar position in the plane of the sky. Therefore, these components are almost outside the beam, and do not have effective contributions in these PV diagrams. With the face-on configuration ($i = 0°$), a velocity gradient due to the rotation motion cannot be seen regardless of $r_{\rm CB}$. Although the PV diagrams with $r_{\rm CB}$ of 10 au is not smooth like those for larger $r_{\rm CB}$, this feature does not have any kinematical meaning, but is due to an artificial effect of the insufficient size of the mesh.

Figure 3.8 shows the model results of PV diagrams prepared along various position angles (P.A.) at various i. The P.A.s are taken for every 30°. The P.A.s of '90°' and

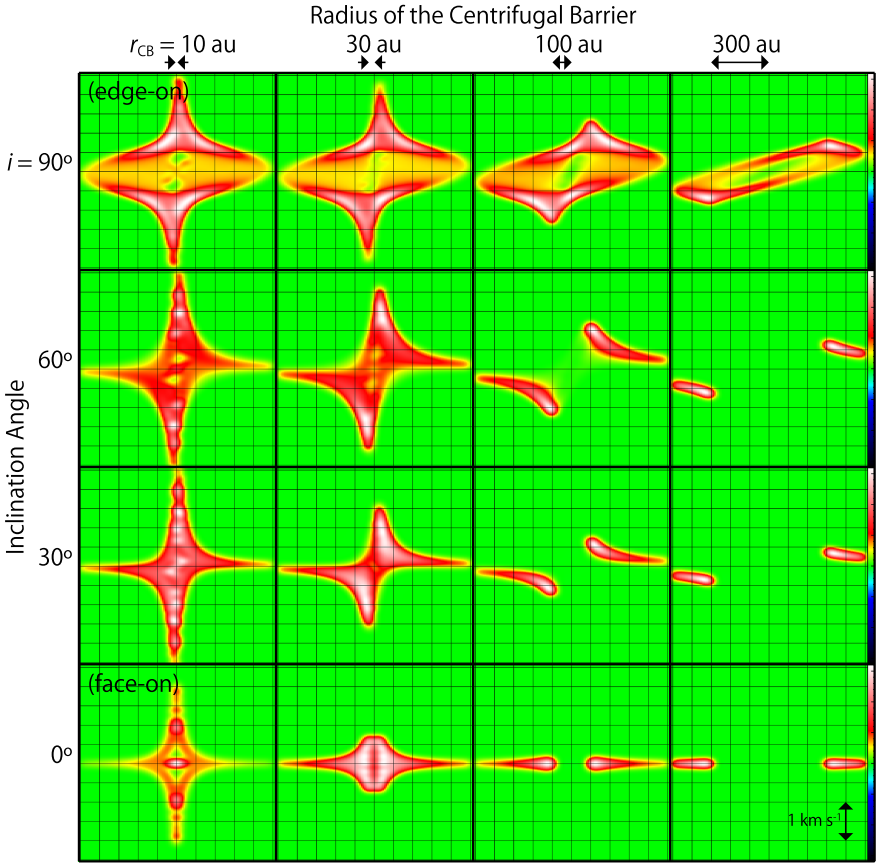

Fig. 3.7 PV diagrams of the infalling-rotating envelope model with various sets of r_{CB} and i. Their position axis is along the arrow (P.A. 90°) shown in Fig. 3.6. It is the direction along which the disk/envelope system is extended. The other physical parameters are set to be as the same as those in Fig. 3.5

'180°' represent the direction along which the mid-plane of the envelope is extended and one perpendicular to it, respectively. The FWHM value of the Gaussian beam is 0.″5 (50 au). The other physical parameters are summarized in the caption. With the edge-on configuration (i = 90°), the distributions look concentrated around the protostar in the PV diagrams with the P.A. of (120° − 240°). A slight velocity gradient can be seen for these P.A.s, except for the P.A. of 180° (the direction perpendicular to the envelope). The velocity shift in the diagram with the P.A. of 180° is due to the infall motion, and it is smaller than that of the rotation motion at the centrifugal barrier. At i of 30° and 60°, the velocity structure changes from P.A. to P.A. The value of the velocity shift is determined by the complex combination of the rotation and infall motions. As shown in Fig. 3.6, the rotation and infall motions cancel each other

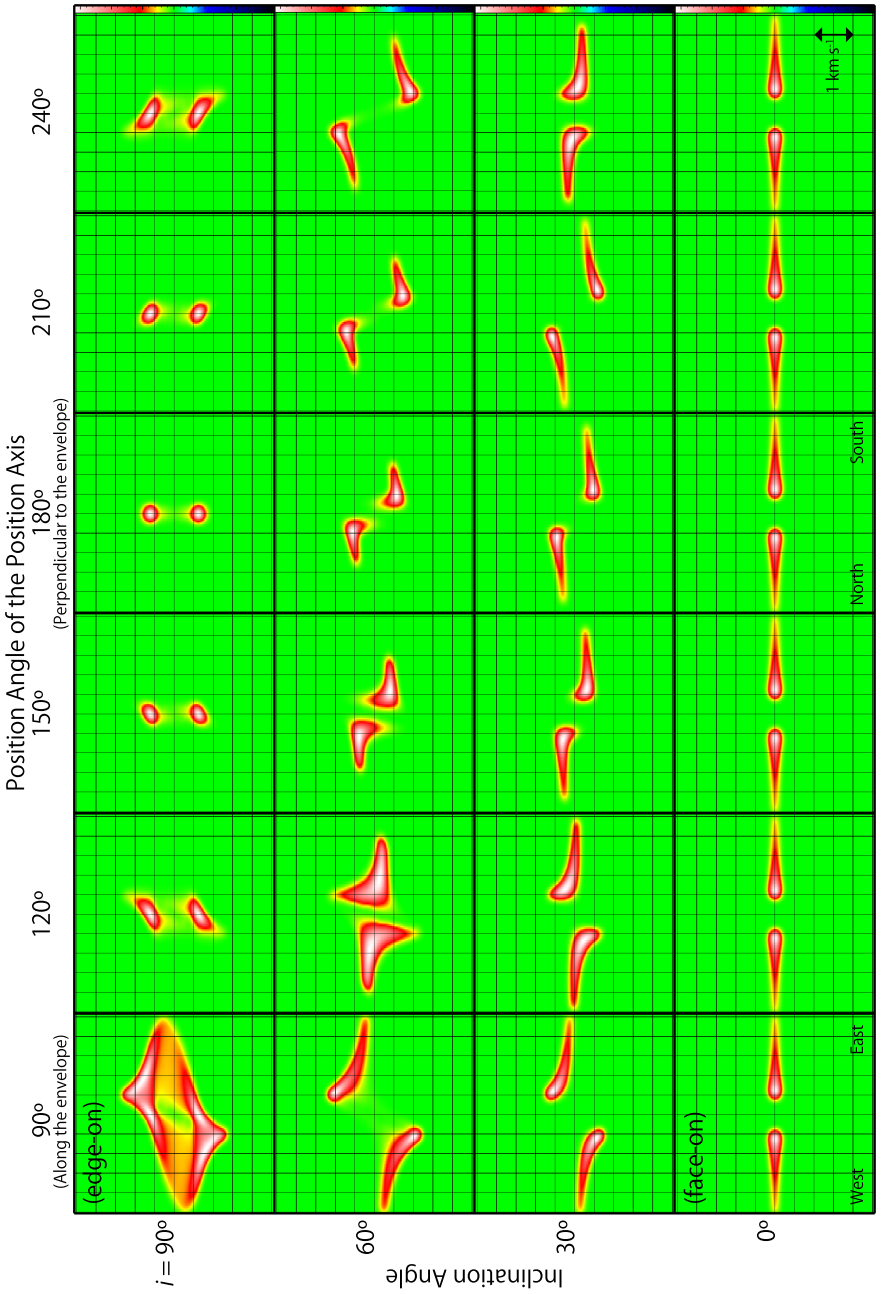

Fig. 3.8 PV diagrams of the infalling-rotating envelope model with various i, where the physical parameters are as follows; $M = 0.1\ M_{\odot}$, $r_{\rm CB} = 100$ au, and $R = 500$ au. The position axes are taken for every 30° from the envelope direction (P.A. 90°)

in the northwestern and southeastern sides of the protostar, while they strengthen each other in the northeastern and southwestern sides. Because of this, the absolute values of the velocity shift tend to be higher in the diagrams with the P.A. of 210° and 240°, where the position axis is along the northeast-southwest direction, than those with the P.A. of 120° and 150°, where the position axis is along the northwest-southeast direction. With the face-on configuration (i of 0°), no velocity gradient can be seen regardless of the P.A.

In Fig. 3.9, the effects of the other physical parameters, such as the protostellar mass (M), the outer radius of the envelope (R), and its scale height, are examined. Although the absolute velocity-shift is larger for larger M, the essential feature of the PV diagrams is not largely affected by M. With a smaller R, the spin-up feature and the counter velocity components are less clear, although the velocity gradient between the centrifugal barriers can be seen. The scale height of the envelope (H)

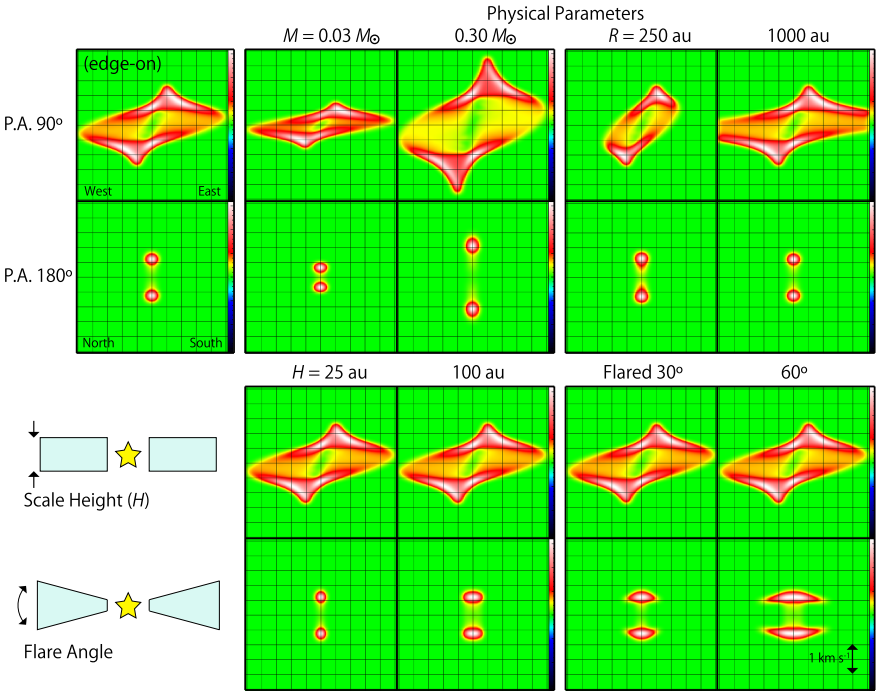

Fig. 3.9 PV diagrams of the infalling-rotating envelope model, whose position axes are along the arrows (P.A. 90° and 180°) shown in Fig. 3.6. The left upper panels show the results of the fiducial model with the following physical parameters; $M = 0.1\ M_{\odot}$, $r_{\rm CB} = 100$ au, $i = 90°$ (edge-on), $R =$ 500 au, and H of 50 au independent of the radius. In the other panels, one of the following physical parameters is changed; the protostellar mass M (0.03 and 0.3 $M_{\odot}$), the outer radius of the envelope R (250 and 1000 au), and the scale height of the envelope H (25 and 100 au). The scale height is assumed to be independent of the radius, or assumed to increase as the radius ('flared') with the flare angle of 30° and 60°

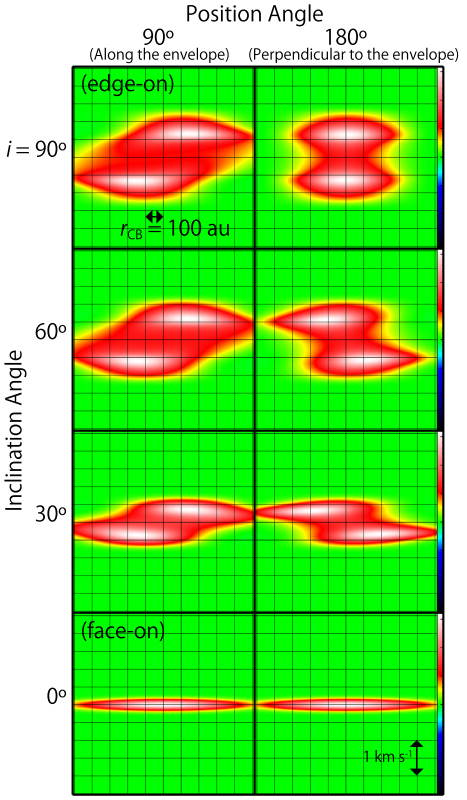

Fig. 3.10 PV diagrams of the infalling-rotating envelope model with various set of i and the position angle, where the other physical parameters are as follows; $M = 0.1\ M_{\odot}$, $r_{\rm CB} = 100$ au, $R = 500$ au, and $H = 50$ au. The position angles of the line along which the position-velocity diagram is prepared are along the mid-plane of the envelope and perpendicular to it in the left and right panels, respectively. The intensity is convolved with the Gaussian beam of $5'' \times 5''$

does not seriously affect the appearance of the PV diagrams with a P.A. of 90° (along the mid-plane extension). With the edge-on configuration, the scale height affects the distribution along the direction perpendicular to the mid-plane extension (P.A. 180°).

Figure 3.10 shows how the appearance of the model results changes with a large beam size ($5''$). The centrifugal barrier ($r_{\rm CB} = 100$ au) is not spatially resolved enough with the beam (500 au). The velocity gradient due to the rotation motion is recognized for the cases at i of ($30° - 90°$). Although the counter velocity components cannot be seen with i of 30° and 60° with a beam of $0.''5 \times 0.''5$ in Fig. 3.7, they are seen in Fig. 3.10. Since the beam is larger than the apparent distance between the centrifugal barriers in these models, the emission of the infalling gas contributes to the PV diagrams. A similar effect due to the large beam is also seen in the PV diagrams along the direction perpendicular to the envelope; the rotating gas at the centrifugal barrier contributes to these diagrams, and hence, the maximum velocity-shift is as high as the maximum rotation velocity at the centrifugal barrier. In these diagrams, disentanglement of the rotation and infall motion is difficult. In the observational studies, it also makes difficult to find the position angle of the extension of the envelope component. Higher angular-resolution observations are always essential.

3.3 Keplerian Model

In Chaps. 6 and 8, the Keplerian disk model is employed to simulate the disk component. The velocity of the gas at the radius r from the protostar are represented as:

$$v_{\rm Kep} = \sqrt{\frac{GM}{r}}, \quad v_{\rm fall} = 0. \tag{3.6}$$

As shown in Fig. 3.2, the Keplerian velocity takes the lower value than $v_{\rm rot}$ by a factor of $\sqrt{2}$ in the above infalling-rotating envelope model at the centrifugal barrier ($r = r_{\rm CB}$), while it equals to $v_{\rm rot}$ in the infalling-rotating envelope model at the centrifugal radius ($r = 2r_{\rm CB}$).

Figure 3.11 shows the integrated intensity map (moment 0 map), velocity field (moment 1 map), and PV diagrams of the Keplerian model. In these models, the protostellar mass and the outer radius of the Keplerian disk are assumed to be 0.1 $M_\odot$ and 500 au, respectively. The constant scale height of 50 au is assumed. The FWHM value of the Gaussian beam is $0.''5$ (50 au).

In the integrated intensity (moment 0) maps, the distributions seem to be compact and concentrated around the protostar. Since the density of the gas is assumed to be proportional to $r^{-1.5}$, the contributions from the vicinity of the protostar are dominant. In the maps of the velocity field (moment 1 maps), the rotation motion is clearly shown. No skewed feature is seen in the moment 1 maps. In the PV diagrams along the envelope (P.A. 90°), the spin-up feature can be confirmed, except for the model with a face-on configuration. No counter velocity component which is seen in the infalling-rotating envelope model is seen in the Keplerian model, because there is no infall motion. In the PV diagrams along the direction perpendicular to the envelope (P.A. 180°), no velocity gradient is seen regardless of i. High velocity components seen in the panels for i of 30° and 60° in Fig. 3.11d are the contamination of the rotation motion near the protostar due to the finite beam size.

3.4 Outflow Model

As well as the disk/envelope system, the kinematic structure of outflows are investigated. The parabolic outflow model from [4] is employed to analyze the observed geometrical and kinematical structures of the outflow. This is just a morphological model. This parabolic model is widely applied to various low-mass and high-mass protostellar sources (e.g. [1, 2, 5, 14, 15, 17, 18]).

In this model, the outflow cavity is assumed to have a parabolic shape and its velocity is proportional to the distance to the protostar. The shape of the outflow cavity wall and the velocity of the gas on the cavity wall are represented as follows:

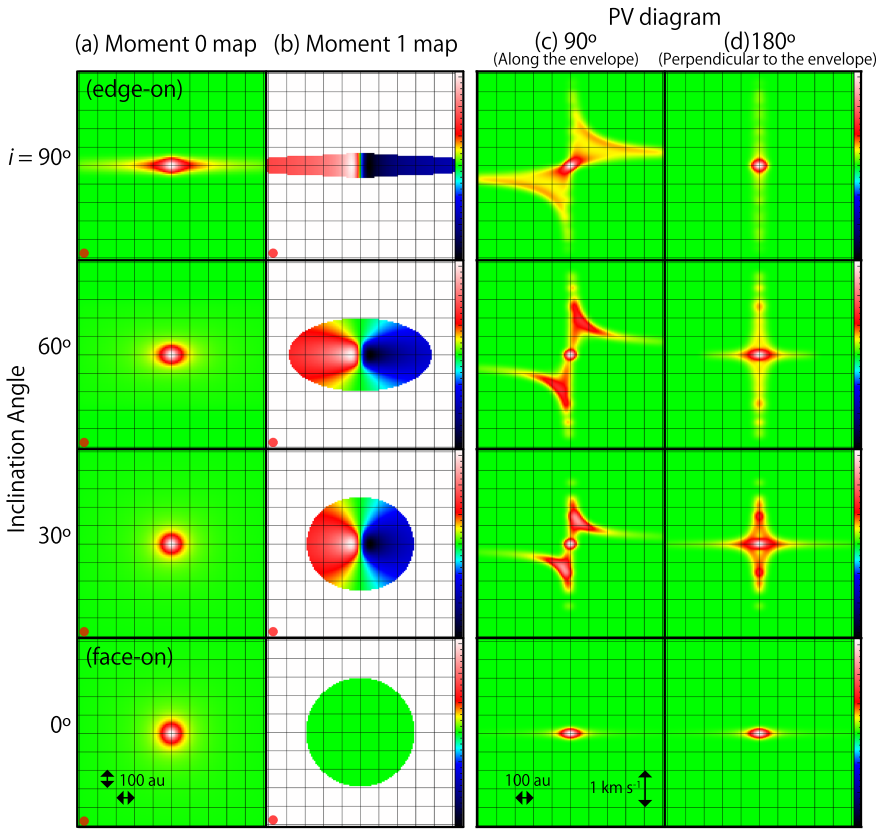

Fig. 3.11 **a** Integrated intensity maps, **b** maps of the velocity field, and **c**, **d** PV diagrams of the Keplerian model. The position axes in panels (**c**) and (**d**) are as the same as those in Fig. 3.10. The physical parameters are as follows; $M = 0.1\ M_{\odot}$, $R = 500$ au, and $H = 50$ au. The intrinsic line width and the beam size are 0.2 km s^{-1} and 0.″5, respectively, which are the same as those in Figs. 3.5, 3.6, 3.7, 3.8 and 3.9

$$z = CR^2, \quad v_R = v_0 \frac{R}{R_0}, \quad v_z = v_0 \frac{z}{z_0}, \tag{3.7}$$

where the z axis is taken along the outflow axis with an origin at the protostar, and R denotes the radial size of the outflow cavity perpendicular to z-axis. R_0 and z_0 are normalization constants, and both are set to be 1 au. C and v_0 are free parameters. Thus, the outflow cavity wall has a parabolic shape in this model, and it is linearly accelerated as the distance from the protostar along the outflow axis (z) and that from the outflow axis (R). In this model, the distribution of the gas is artificially assumed to be uniform for all data points, where the mass of the outflowing gas is not conserved along z-axis. An optically thin condition is also assumed, where the intensity of the line emission is proportional to the column density along the line of sight. These

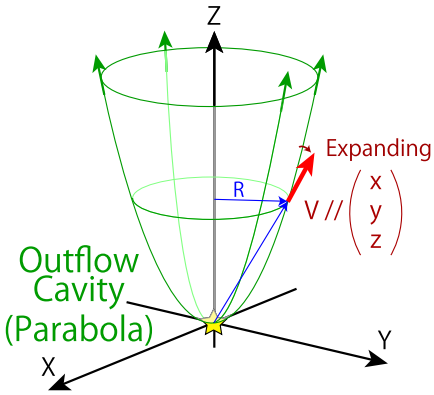

Fig. 3.12 Schematic illustration of the parabolic outflow model

simplified assumptions are employed in this study, because the main interest in the model analysis is on the velocity profile. Since the extended component would be resolved-out, it is difficult to derive accurate density profile from the observations with the interferometer. Therefore, the emissivity is not considered in the outflow analysis.

Figure 3.12 shows the schematic illustration of this model. Figure 3.13 shows how sensitive to the physical parameters the model results are in their integrated intensity map (moment 0 map), the map of the velocity field (moment 1 map), and the PV diagrams. In these models, the outflow axes are assumed to be along the north-south axis. The two outflow lobes blow in parallel to the plane of the sky with i of 90°, while they are nearly pole-on for the case at i of 30°. In each PV diagram, two parabolic features are seen. One parabolic feature corresponds to one outflow lobe. With smaller C, the parabolic features show larger opening angles. For the case at i of 90°, the gas on the outflow cavity wall shows both a red- and blue-shifted velocity at one position. These are the contributions from two positions on the cavity wall in front of and behind the outflow axis. These velocity shifts have the same absolute value. With i of 30° and 60°, the symmetric axis of the parabolic feature is red- and blue-shifted in the northern and southern sides of the protostar, respectively. Thus they can be called as the 'red-shifted lobe' or 'blue-shifted lobe'. The sign of the velocity shift is determined by the combination of the inclination angle and the curvature of the lobes. As a result, there are some parts showing a counter velocity-shift to the symmetric axis. Some parts of a lobe can appear in the counter side to the outflow axis with respect to the protostellar position. It can be confirmed as a parabolic feature which crosses the protostellar position in the PV diagram.

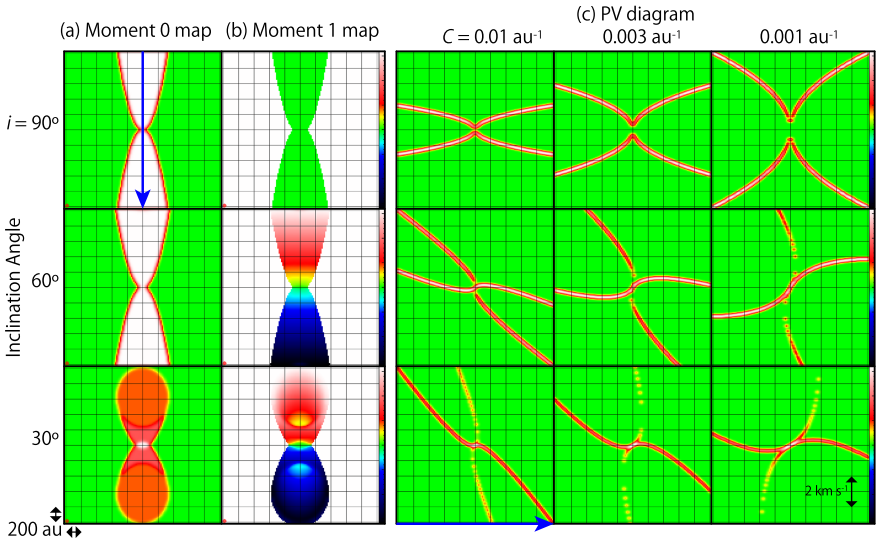

Fig. 3.13 **a** Integrated intensity maps and **b** maps of the velocity field of the outflow model with various i. The parameters of the curvature (C) and the velocity (v_0) are fixed to be 0.01 au^{-1} and 0.5 km s^{-1}. **c** PV diagrams of the outflow model along the outflow axis with various i and the curvature C (au^{-1}). The position axis is along the blue arrow shown in panel (**a**) for i of 90°. The parameter of the velocity (v_0) is fixed to be 0.5 km s^{-1}, where the velocity is 0.5 km s^{-1} at the distance of 1 au from the protostar

3.5 Physical Parameters of the Models

In the models described in Sects. 3.2–3.4, there are some key free parameters while some physical parameters are fixed. They are summarized in Table 3.1.

3.6 Examples of the Model Analysis

3.6.1 The L1527 Case

The infalling-rotating envelope model explained in Sect. 3.2 was first applied for L1527 [10]. L1527 is a low-mass protostellar core in Taurus (d = 137 pc [16]). The details of L1527 are described in Chap. 4.

[10] reported the high angular-resolution observations toward L1527 with ALMA. Figure 3.14a shows the integrated intensity maps of CCH and c-C_3H_2 toward L1527. The envelope component is seen to be extended along the north-south axis. Figure 3.14b shows the position-velocity (PV) diagram of CCH along the north-south axis centered at the protostellar position represented by the white cross

Table 3.1 Free and fixed physical parameters in the models

Physical parameter	Free or Fixed
Infalling-Rotating Envelope Model	
Distance (d)	Fixed (See Table 1.1)
Protostellar mass (M)	Free
Inclination angle (i)	Fixed (The value from references or derived from the outflow analysis)
Radius of the centrifugal barrier (r_{CB})	Free
Outer radius (R)	Free
Scale height of the envelope	Fixed (Uniformed or proportional to the distance from the protostar)
Beam size	Fixed based on the observations
Intrinsic line width	Fixed
Emissivity[a]	Fixed ($\propto r^{-1.5}$)
Mesh size	Fixed
Keplerian Model	
Distance (d)	Fixed (See Table 1.1)
Protostellar mass (M)	Fixed (The value derived from the envelope analysis)
Inclination angle (i)	Fixed (The same value in the envelope analysis)
Outer radius of the disk (R)	Fixed to be r_{CB}
Beam size	Fixed based on the observations
Intrinsic line width	Fixed
Emissivity[a]	Fixed ($\propto r^{-1.5}$)
Mesh size	Fixed
Outflow Model	
Distance (d)	Fixed (See Table 1.1)
Inclination angle (i)	Free (0° for a pole-on configuration)
Curvature (C)	Free
Velocity (v_0)	Free
Beam size	Fixed based on the observations
Intrinsic line width	Fixed
Emissivity[b]	Fixed to be uniform
Mesh size	Fixed

[a] In reality, the intensity of the line emission from each data point is determined by the combination of several physical conditions; e.g. the H_2 density ($n(H_2)$), the abundance ratio of the molecule to H_2 ($f(X)$), the gas temperature. In this model, the intensity is simply assumed to be proportional to the column density, where $n(H_2)$ is assumed to be proportional to $r^{-1.5}$ (an infalling envelope; e.g. [3, 6, 13]), $f(X)$ is constant, and the temperature does not affect the emissivity

[b] In this chapter, the density of the molecule in the outflow model is simply assumed to be constant for all data points, because only the velocity structure is focused on in this study. In the actual analyses of the observational data (Chaps. 4, 5 and 8), only the outline of the outflow model is considered

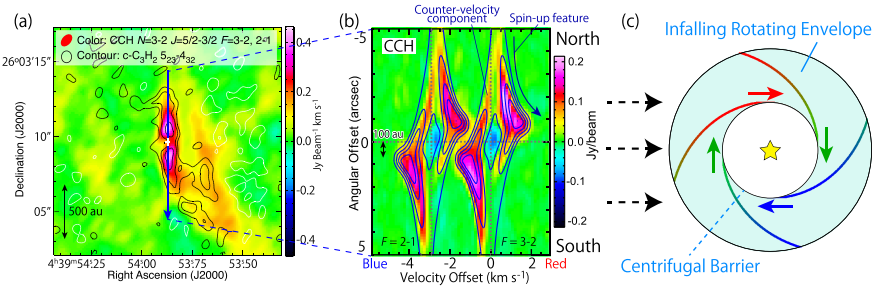

Fig. 3.14 **a** Integrated intensity maps of the CCH ($N = 3 - 2$, $J = 5/2 - 3/2$, $F = 3 - 2$ and $2 - 1$; color) and c-C_3H_2 ($5_{23} - 4_{32}$; contours) lines. Contours levels are -6, -3, 3, 6, and 12 σ, where σ is 6.5 mJy beam^{-1} km s^{-1}. White contours represent a negative intensity. The white cross represents the position of the 0.8 mm continuum peak. **b** Position-velocity diagram of the CCH line prepared along the blue arrow shown in panel (**a**), along which the mid-plane of the disk/envelope system is extended. The hyperfine component ($F = 2 - 1$) is seen with the velocity offset of -2.8 km s^{-1}, and the same structure is repeated twice. Blue contours represent the results of the infalling-rotating envelope model. The physical parameters for the model are as follows; the protostellar mass $M = 0.18\ M_\odot$, the radius of the centrifugal barrier $r_{CB} = 100$ au, and the inclination angle $i = 85°$ (0° for a face-on configuration). Contour levels are every 20% of the peak intensity. **c** Schematic illustration of the infalling-rotating envelope model. Panels (**a**) and (**b**) are taken from [10] with a slight modification. © AAS. Reproduced with permission

in Fig. 3.14a. The velocity of the gas is red- and blue-shifted at the northern and southern sides of the protostar, respectively. A clear spin-up feature is seen in the PV diagram; the velocity shift increases as approaching to the protostar. The CCH emission abruptly disappears at the distance of 100 au from the protostar. There are also seen the components with the inverse velocity of the spin-up feature ('*counter-velocity component*'). The results of the infalling-rotating envelope model are represented as blue contours in Fig. 3.14b. The physical parameters for the infalling-rotating envelope model are as follows; the protostellar mass is 0.18 $M_\odot$, the radius of the centrifugal barrier is 100 au, and the inclination angle of the disk/envelope system is 85° (0° for a face-on configuration). The model results well reproduce the observed kinematic structures of the CCH lines, including the counter-velocity component.

3.6.2 The TMC−1A Case

Another example is the TMC−1A case. This source is located in the Heiles Cloud 2 ($d = 137$ pc [16]), which harbors the low-mass Class I protostar IRAS 04365+2535. It shows the chemical characteristic of WCCC similar to L1527 [12]. [9] conducted high angular-resolution observations of the CS ($J = 5 - 4$) and SO ($J_N = 7_6 - 6_5$) lines toward this source with ALMA (Fig. 3.15). The kinematic structure in the vicinity of the protostar can be explained by the above infalling-rotating envelope

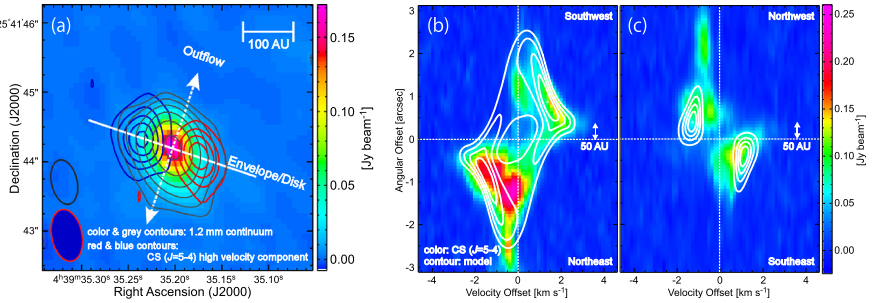

Fig. 3.15 **a** 1.2 mm continuum map (color, gray contours) and the integrated intensity maps of the high velocity components of CS ($J = 5 - 4$; red and blue contours) in TMC−1A. **b**, **c** PV diagrams of CS ($J = 5 - 4$) along the envelope direction (**b**) and the line perpendicular to it (**c**). The position axes are represented by the white line and arrow in panel (**a**). Taken from [9]. © AAS. Reproduced with permission

model (Fig. 3.15b), where the physical parameters are M of 0.25 $M_{\odot}$ and r_{CB} of 50 au. Figures 3.15 show the PV diagrams of CS prepared along the envelope direction and the line perpendicular to it. Although some parts of the molecular distributions seem to be missing due to the asymmetric gas distribution, the results of the infalling-rotating envelope model shown in white contours reasonably explain the kinematic structures. Thus, the infalling-rotating envelope model is expected to be a powerful tool to examine the essential kinematics in the disk forming region.

3.6.3 Some Caveats for the Model

As demonstrated in the L1527 case (Fig. 3.14), the observed kinematic structures are investigated by comparing with the physical models. The infalling-rotating envelope model is a quite simplified one as described in Sect. 3.2.1: the model does not consider any excitation effects, radiative transfer effects, and abundance variations of molecules. However, in reality, some parts of the envelope gas can be optically thick, and the distribution itself can be asymmetric around the protostar. Thus, it is not fruitful to make a fine tuning of the model so as to better match with the observed intensity. Therefore, the fundamental characteristics of the kinematic structure is focused on in this thesis. Hence, model simulations are conducted with a wide range of physical parameters, and their reasonable ranges are basically evaluated by eye. In model analyses, chi-squared tests are often employed to derive reliable values for the model parameters [8]. However, chi-squared tests for the infalling-rotating envelope model are not conducted in this thesis, considering the overwhelming systematic errors caused by the simplified assumptions described above.

References

1. Arce HG, Mardones D, Corder SA, Garay G, Noriega-Crespo A, Raga AC (2013) ALMA observations of the HH 46/47 molecular outflow. ApJ 774(1):39
2. Beuther H, Schilke P, Gueth F (2004) Massive molecular outflows at high spatial resolution. ApJ 608(1):330–340
3. Harvey DW, Wilner DJ, Myers PC, Tafalla M, Mardones D (2003) Inner structure of protostellar collapse candidate B335 derived from millimeter-wave interferometry. ApJ 583(2):809–818
4. Lee C-F, Mundy LG, Reipurth B, Ostriker EC, Stone JM (2000) CO outflows from young stars: confronting the jet and wind models. ApJ 542(2):925–945
5. Lumbreras AM, Zapata LA (2014) SMA submillimeter observations of HL Tau: revealing a compact molecular outflow. AJ 147(4):72
6. Ohashi N, Hayashi M, Ho PT, Momose M (1997) Interferometric imaging of IRAS 04368+2557 in the L1527 molecular cloud core: a dynamically infalling envelope with rotation. ApJ 475(1):211–223
7. Oya Y, Sakai N, Sakai T, Watanabe Y, Hirota T, Lindberg JE, Bisschop SE, Jørgensen JK, van Dishoeck EF, Yamamoto S (2014) A substellar-mass protostar and its outflow of IRAS 15398–3359 revealed by subarcsecond-resolution observations of H_2CO and CCH. ApJ 795(2):152
8. Oya Y, Yamamoto S (2020) Substructures in the disk-forming region of the class 0 low-mass protostellar source IRAS 16293–2422 source A on a 10 au scale. ApJ 904(2):185
9. Sakai N, Oya Y, López-Sepulcre A, Watanabe Y, Sakai T, Hirota T, Aikawa Y, Ceccarelli C, Lefloch B, Caux E, Vastel C, Kahane C, Yamamoto S (2016) Subarcsecond analysis of the infalling-rotating envelope around the class I protostar IRAS 04365+2535. ApJ 820(2):L34
10. Sakai N, Oya Y, Sakai T, Watanabe Y, Hirota T, Ceccarelli C, Kahane C, Lopez-Sepulcre A, Lefloch B, Vastel C, Bottinelli S, Caux E, Coutens A, Aikawa Y, Takakuwa S, Ohashi N, Yen H-W, Yamamoto S (2014) A chemical view of protostellar-disk formation in L1527. ApJ 791(2):L38
11. Sakai N, Sakai T, Hirota T, Watanabe Y, Ceccarelli C, Kahane C, Bottinelli S, Caux E, Demyk K, Vastel C, Coutens A, Taquet V, Ohashi N, Takakuwa S, Yen H-W, Aikawa Y, Yamamoto S (2014) Change in the chemical composition of infalling gas forming a disk around a protostar. Nature 507(7490):78–80
12. Sakai N, Sakai T, Hirota T, Yamamoto S (2008) Abundant carbon-chain molecules toward the low-mass protostar IRAS 04368+2557 in L1527. ApJ 672(1):371–381
13. Shu FH (1977) Self-similar collapse of isothermal spheres and star formation. ApJ 214:488–497
14. Takahashi S, Ho PT (2012) The discovery of the youngest molecular outflow associated with an intermediate-mass protostellar core, MMS-6/OMC-3. ApJ 745(1):L10
15. Takahashi S, Ohashi N, Bourke TL (2013) Direct imaging of a compact molecular outflow from a very low luminosity object: L1521F-IRS. ApJ 774(1):20
16. Torres RM, Loinard L, Mioduszewski AJ, Rodríguez LF (2007) VLBA Determination of the distance to nearby star-forming regions. II. Hubble 4 and HDE 283572 in Taurus. ApJ 671(2):1813–1819
17. Yeh SC, Hirano N, Bourke TL, Ho PT, Lee CF, Ohashi N, Takakuwa S (2008) The CO molecular outflows of IRAS 16293-2422 probed by the submillimeter array. ApJ 675(1):454–463
18. Zapata LA, Arce HG, Brassfield E, Palau A, Patel N, Pineda JE (2014) A spider-like outflow in Barnard 5 - IRS 1: the transition from a collimated jet to a wide-angle outflow? MNRAS 441(4):3696–3702